Sol–Gel Synthesis and Electrospraying of Biodegradable $(P_2O_5)_{55}-(CaO)_{30}-(Na_2O)_{15}$ Glass Nanospheres as a Transient Contrast Agent for Ultrasound Stem Cell Imaging

Farzad Foroutan,[†,‡,⊗] Jesse V. Jokerst,[§,⊗] Sanjiv S. Gambhir,[§] Ophir Vermesh,[§] Hae-Won Kim,[∥,⊥,#] and Jonathan C. Knowles*[,†,#]

[†]Division of Biomaterials and Tissue Engineering/Eastman Dental Institute, University College London, 256 Gray's Inn Road, London WC1X 8LD, U.K., [‡]Department of Chemistry/Faculty of Math and Physical Science, University College London, 20 Gordon Street, London WC1H 0AJ, U.K., [§]Molecular Imaging Program at Stanford (MIPS), Department of Radiology, Stanford University, 318 Campus Drive, Stanford, California 94305-5427, United States, [∥]BK21 PLUS NBM Global Research Center for Regenerative Medicine, [⊥]Institute of Tissue Regeneration Engineering (ITREN), and [#]Department of Nanobiomedical Science and WCU Research Centre of Nanobiomedical Science, Dankook University, Cheonan 330-714, Republic of Korea. [⊗]F.F. and J.V.J. contributed equally to this work.

ABSTRACT Ultrasound imaging is a powerful tool in medicine because of the millisecond temporal resolution and submillimeter spatial resolution of acoustic imaging. However, the current generation of acoustic contrast agents is primarily limited to vascular targets due to their large size. Nanosize particles have the potential to be used as a contrast agent for ultrasound molecular imaging. Silica-based nanoparticles have shown promise here; however, their slow degradation rate may limit their applications as a contrast agent. Phosphate-based glasses are an attractive alternative with controllable degradation rate and easily metabolized degradation components in the body. In this study, biodegradable $P_2O_5-CaO-Na_2O$ phosphate-based glass nanospheres (PGNs) were synthesized and characterized as contrast agents for ultrasound imaging. The structure of the PGNs was characterized using scanning electron microscopy (SEM), energy-dispersive X-ray spectroscopy (EDX), X-ray diffraction (XRD), ^{31}P magic angle spinning nuclear magnetic resonance (^{31}P MAS NMR), and Fourier transform infrared (FTIR) spectroscopy. The SEM images indicated a spherical shape with a diameter size range of 200–500 nm. The XRD, ^{31}P NMR, and FTIR results revealed the amorphous and glassy nature of PGNs that consisted of mainly Q^1 and Q^2 phosphate units. We used this contrast to label mesenchymal stem cells and determined *in vitro* and *in vivo* detection limits of 5 and 9 μg/mL, respectively. Cell counts down to 4000 could be measured with ultrasound imaging with no cytoxicity at doses needed for imaging. Importantly, ion-release studies confirmed these PGNs biodegrade into aqueous media with degradation products that can be easily metabolized in the body.

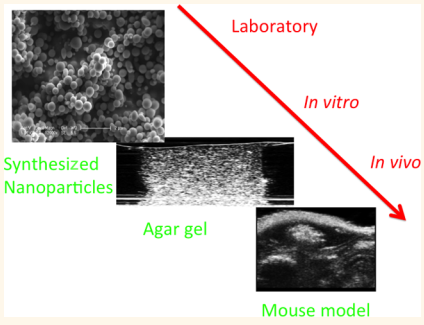

KEYWORDS: sol–gel · electrospraying · phosphate-based glasses · ultrasound imaging

Ultrasound imaging is a real time, low cost, nonionizing, and effective imaging tool yet remains primarily an anatomic tool *versus* positron emission tomography (PET) or bioluminescence. While ultrasound contrast agents can increase the signal specificity for molecular imaging by increasing backscattered echoes from the target site, the current generation of microbubbles are too large to be used outside of the vasculature or inside specific cells of interest.[1−4] Microbubbles were first introduced as a contrast agent in 1968 by injecting agitated saline into the ascending aorta and cardiac chambers during echocardiographic examination.[5] Strong echoes were produced within the heart, due to the acoustic mismatch between free air microbubbles in the saline and the surrounding blood. However, microbubbles

* Address correspondence to j.knowles.ucl.ac.uk.

Received for review November 28, 2014 and accepted January 27, 2015.

Published online January 27, 2015
10.1021/nn506789y

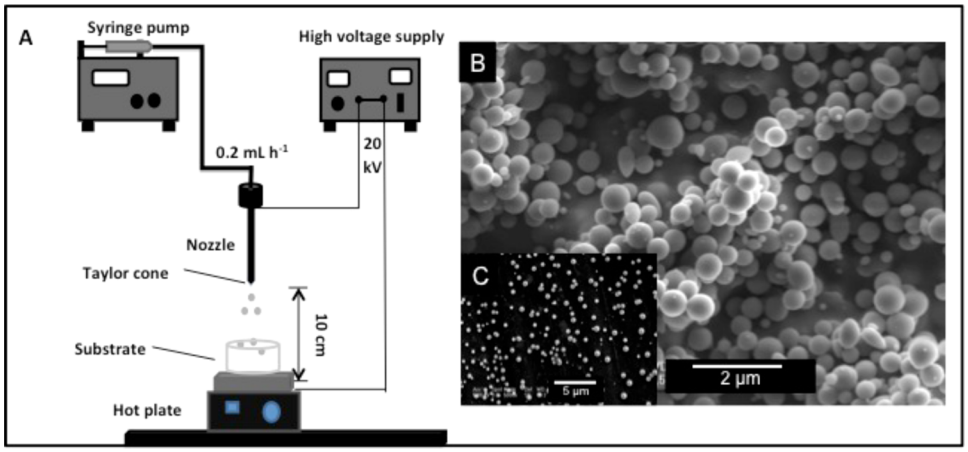

Figure 1. (A) Schematic of the electrospraying setup. The high voltage between the nozzle and the ground-created nanospheres that flew toward the heated silicone oil as a substrate to obtain dried gel nanospheres. SEM image of (B) washed and heat-treated PGNs (the scale bar is 2 μm) and (C) dispersed PGNs in ethanol solution after heat treatment (the scale bar is 5 μm). The PGNs have an approximate size range of between 200 and 500 nm with mean diameter size of 320 nm (N = 100 particles).

produced by agitation are both large and unstable and diffuse into solution in a short period of time.

To overcome these limitations, encapsulated gas bubbles were invented; however, these microbubbles are unstable in circulation even with polyethylene glycol surface treatment.[6−8] Furthermore, microbubbles require a careful choice of ultrasound frequency because microbubbles burst at low frequencies that can result in local microvasculature rupture and hemolysis.[9] While nanobubbles have made important improvements in this area, a complete solution has remained elusive.[10−12]

One alternative is solid nanoparticles that have utility as backscatter contrast agents for ultrasound molecular imaging.[13−15] These solid particles have been used to image stem cells in cardiac regenerative medicine or to image cell surface proteins in cancer cells.[13,14] However, the material properties of these agents are critical. They must have acoustic impedance capable of strongly and stably backscattering incident acoustic energy but also be metabolized and removed safely from the body shortly thereafter. Finally, the particles must be small enough to extravasate from tumor vasculature due to the enhanced permeation and retention effect or be phagocytosed by cells when growing in culture. While silica-based nanoparticles have shown promise here,[16−18] phosphate-based glasses are an attractive alternative because they offer a controllable degradation rate by varying their chemical compositions and which give rise to easily metabolized degradation components in the body.[19−21]

Previous approaches to preparing ternary phosphate-based glasses in the P_2O_5−CaO−Na_2O system *via* a sol−gel synthesis method have focused on preparing bulk sol−gel glasses.[22,23] However, because of the slow reaction of the phosphate precursors, the reaction times were long. In addition, subsequent high-drying temperatures made it difficult to prepare bulk glasses suitable for biomedical applications.

Here, we report a new simplified sol−gel synthesis method to prepare a ternary P_2O_5−CaO−Na_2O glass system at low temperature with subsequent electrospraying to obtain nanospherical glasses. The PGNs were characterized by scanning electron microscopy (SEM), energy-dispersive X-ray spectroscopy (EDX), X-ray diffraction (XRD), ^{31}P nuclear magnetic resonance (^{31}P MAS NMR), and Fourier transform infrared (FTIR) spectroscopy as well as *in vitro* and *in vivo* ultrasound imaging. Biodegradation was then monitored *via* inductively coupled plasma mass spectroscopy (ICP-MS) to measure phosphorus, calcium, and sodium ion release into aqueous media. We then used these tools to labeled mesenchymal stem cells (MSCs) and studied the effect the contrast agents had on cell viability as well as the signal increases generated by the PGNs. To the best of our knowledge, this is the first report of sol−gel synthesis and electrospraying to prepare biodegradable PGNs at low temperature and the first use of such a system for imaging purposes.

RESULTS

SEM and EDX. We successfully synthesized the nanoparticles with an electrospraying technique (Figure 1A). The shape and particle size of the particles were identified by SEM images. Parts B and C of Figure 1 show nanospherical particles, and measurement of the particle size for more than 100 particles confirmed more than 80% of the particles had a diameter size distribution of 200−500 nm with a mean diameter size of 320 nm. The EDX results were also converted to mol % to allow comparison to be made with the theoretical composition and are reported in Table 1. The results show a reduction of around 12.5 mol % of P_2O_5 content from the theoretical values, with a concomitant increase in the percentage content of the other oxides to compensate. This reduction can be related to the unreacted phosphorus that is lost during the heating stages.

TABLE 1. Intended Compositions and Measured Values Determined by EDX (in Parentheses)

composition (mol %)	P_2O_5	CaO	Na_2O
$(P_2O_5)_{55}$-$(CaO)_{30}$-$(Na_2O)_{15}$	55.0(42.5 ± 1.0)	30.0 (37.9 ± 0.9)	15.0 (19.6 ± 0.8)

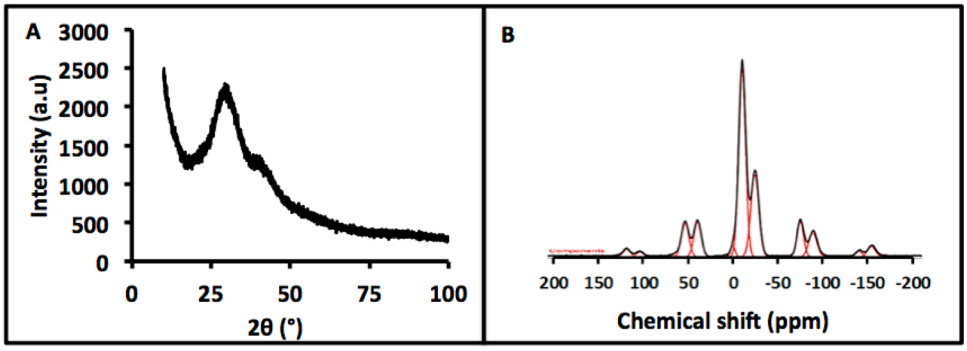

Figure 2. (A) XRD pattern of the PGNs indicate that it is free from any detectable crystalline phase and (B) ^{31}P MAS NMR spectrum (black line) and the fitting (red line) that correspond to mainly Q^1 and Q^2 phosphate units.

TABLE 2. ^{31}P MAS NMR Peak Parameters of the PGNs

position (ppm) (±1.0)	Q^i species	line width (ppm) (±2.0)	abundance (%) (±1.0)
1.7	0	6.7	1.9
−8.3	1	10.1	59.5
−21.9	2	12.5	38.6

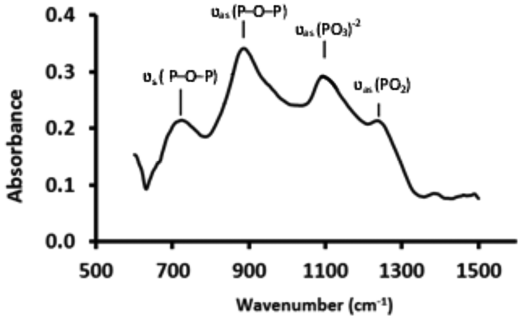

Figure 3. FTIR spectrum and band assignment for PGNs (υ, stretching; s, symmetric; as, asymmetric; δ, deformation).

XRD and ^{31}P MAS NMR. The XRD pattern of the PGNs was free of any detectable crystalline phase (Figure 2A). Only two broad peaks at 2θ values between 20 and 50° were observed. This confirmed the amorphous nature of PGNs.

Figure 2B shows the solid-state ^{31}P MAS NMR spectrum from PGNs. The peak at 1.7 ppm corresponds to the presence of Q^0 phosphate units that can be related to unreacted phosphorus in the structure.[23] The peaks with the chemical shifts at −8.3 and −21.9 ppm are assigned to Q^1 and Q^2 units, respectively (Table 2).[23,24]

FTIR. Figure 3 presents FTIR data for PGNs that allow assignment according to the previous FTIR studies on phosphate-based glasses.[22,25−29] The peak at 730 cm^{-1} can be assigned to the symmetrical stretching υ_s (P−O−P) mode, while the peak at 900 cm^{-1} can be assigned to the asymmetrical stretching υ_{as} (P−O−P) mode (Q^2 phosphate units). The peaks at 1100 and 1235 cm^{-1} are also assigned to asymmetrical υ_{as} $(PO_3)^{-2}$ and υ_{as} (PO_2) modes that can be related to Q^1 and Q^2 phosphate units, respectively.

Ion-Release Study. The concentrations of phosphorus, calcium, and sodium released into solution at different time points are presented in Figure 4. It can be seen that the highest rate of ion release occurs within the first 4 h over the entire study period for all of the elements. It should be noted that there is a small difference between the obtained data from EDX and ICP that can be related to the dissolution behavior of phosphorus that requires the hydrolysis of P−O−P bonds prior to release, whereas other elements may be released *via* diffusion.[30]

Cytotoxicity Study. We measured the cell viability with MTS and studied whether reactive oxygen species were generated with DCFDA (Figure 5). MSCs were used for both applications because of the utility of ultrasound in cardiac stem cell therapy.[14,31] The cells were positive for CD105, CD166, CD29, CD44, CD14, CD34, and CD45 and were below passage no. 5.

The DCFDA assay was first validated with both positive and negative controls. The negative control used wells with no cells plated, and the positive control was wells with MSCs stimulated by 10% hydrogen peroxide. The negative control had a fluorescence value of 297 ± 76, which is attributed to autofluorescence from the plastic well plate. The MSCs in media with neither PGNs nor H_2O_2 had a value of 869 ± 118. The H_2O_2-positive control validated the assay and was 2.2-fold higher than the control cells. The experiments with PGNs added to the MSCs showed no increase in DCFDA signal except at 1000 μg/mL. Here, the signal increased 1.6-fold to 1372 ± 41, a value that was significant at $p < 0.0001$ *versus* the 0 μg/mL control.

All other PGNs concentrations had p values above 0.05 indicating no generation of ROS (Figure 5A).

We also used the MTS assay to measure any effects on cell viability and used two fractions of PGNs; freshly dissolved PGNs in PBS (Figure 5B, fresh) and PGNs that had been in PBS overnight (Figure 5B, degraded). In both cases, cells were treated with increasing concentrations of PGNs. The positive control was the known cytotoxic agent CTAB. Cells without stimulation had an optical density at 490 nm of 0.85 $\pm$ 0.06 for the fresh sample and 0.90 $\pm$ 0.05 for the degraded sample. No concentrations had a statistically significant change to baseline except the positive control, which suppressed the signal 4.3- and 4.1-fold for the fresh and degraded samples, respectively.

***In Vitro* Ultrasound Imaging.** We tested the ability of the PGNs to backscatter acoustic energy with phantoms. Inclusions contain increasing concentrations of PGNs were added to the agarose support and imaged at 40 MHz (Figure 6). In Figure 6A, the echogenicity of a 0 mg/mL water control is seen. The outline of the well can be seen clearly due to the presence of air bubbles that became trapped on the side of the well (green dashed lines). A much more intense signal is seen when an identical well is loaded with 1 mg/mL PGNs (Figure 6B). The mean intensity of this image and at least three replicate images was measured to be 81.5 $\pm$ 1.3 au. This value and the value determined for the other concentrations of PGNs are plotted in Figure 6C. Using the best fit line (R^2 > 0.99) and the background value of 5.3 $\pm$ 0.4, we estimated the limit of detection to be 5 μg/mL at three standard deviations above the mean of the background.

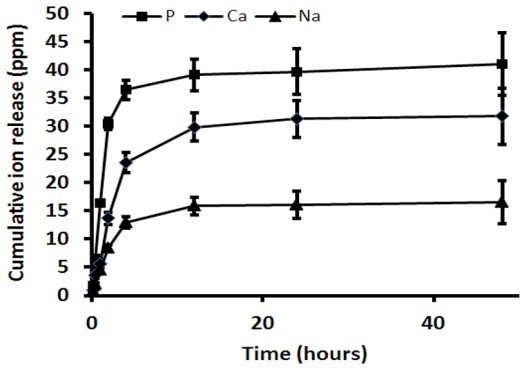

Figure 4. Cumulative release of phosphorus, calcium, and sodium in deionized water as a function of time for the investigated PGNs. Error bars represent the standard deviation of three samples.

To understand how biodegradation affects ultrasound signal, we also imaged samples after different periods of dissolution in standard PBS (Figure 6D). We found that the signal has a maximum near 10 min but remains elevated at least 4 h after wetting. Interestingly, the increase from 2 to 10 min was significant (p < 0.05) and suggests that the wetting of the PGNs may induce hydration that increases backscatter.

The frequency of imaging is also an important parameter. Higher frequencies have better resolution, but lower depth of penetration and the echogencity of the material may change as a function of frequency. To understand how the PGNs behave at both clinical and preclinical frequencies, we also imaged at 16 MHz (Figure 6E). We measured the signal of a 1 mg/mL sample of nanoparticles as well as the background signal of agar. We then plotted both the signal and signal-to-background (S/B) in Figure 6F. While the signal was 36% higher at 40 MHz, the signal-to-background at 16 MHz was 4.6-fold higher than 40 MHz because of a lower background signal. These data indicate that the PGNs are suitable for imaging at a variety of both clinical and preclinical frequencies.

***In Vivo* and Cellular Ultrasound Imaging.** To understand the capability of PGNs for *in vivo* imaging and biodegradation, we implanted 100 μL boluses of increasing concentrations of PGNs onto the rear flank of nude

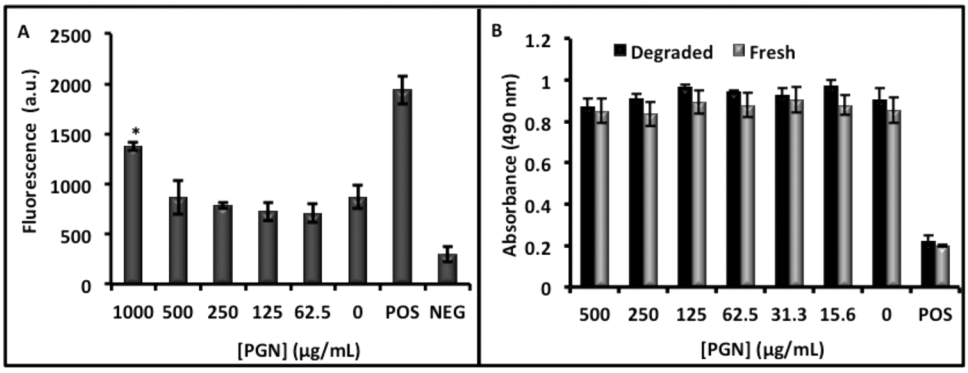

Figure 5. Cytotoxicty data. Increasing concentrations of PGNs were used to label MSCs for 4 h followed by treatment with different markers of cytotoxicity. All experiments were validated with a positive control (POS). (A) Cells were plated, tagged with DCHCF, and then perturbed with PGNs. Any ROS generation resulted in fluorescence from the DCHCF probe. Only the 1000 μg/mL sample significantly upregulated ROS. A hydrogen peroxide positive control validated the assay. The negative control was wells with no cells. (B) MTS reagent measures cell metabolism and showed no decrease at any concentration studied. Here, we used both freshly dissolved PGNs (fresh) and PGNs that had been in solution for 24 h (degraded). No concentration decreased metabolism. Error bars represent the standard deviation of six wells.

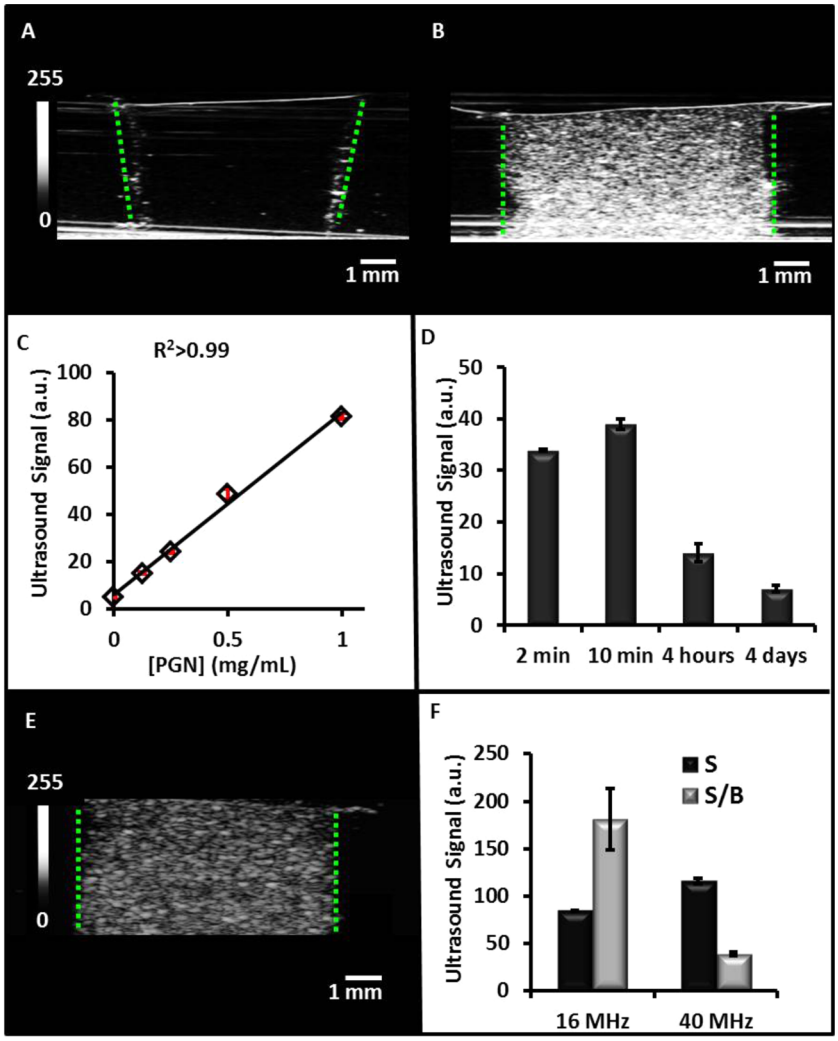

Figure 6. Ultrasound signal performance of the PGNs. Ultrasound images in the *z*-axis for inclusions with 0 mg/mL PGNs (A) and 1 mg/mL PGNs at 40 MHz (B). (C) Increased backscatter results from increasing number of particles that was further quantitated for multiple fields of view. PGNs (0.25 mg/mL) at various time points were imaged with ultrasound to understand how signal changes as a function of time (D). These data indicate that ultrasound signal decreases as the nanoparticle degrades because of decreased acoustic impedance. The imaging window is within the first 4 h of dissolution. (E) Ultrasound image in the *z*-axis for 1 mg/mL PGNs at 16 MHz. (F) Signal and signal-to-background for both 16 and 40 MHz. Here, signal was defined as echogenicity of the sample, and background was adjacent agar. While the signal was higher at 40 MHz, the signal-to-background at 16 MHz was 4.6-fold higher than 40 MHz because of a lower background signal. These data indicate that the PGNs are suitable for imaging at both clinical and preclinical frequencies.

mice (Figure 7A). These samples were in a 50% matrigel carrier, and this vehicle served as the 0 mg/mL or negative control. Each implant was imaged at 40 MHz and the backscatter quantitated for various concentrations in Figure 7C. The calculated limit of detection *in vivo* is 9 μg/mL of PGNs, a value nearly 2-fold higher than *in vitro* analysis. This is because of the increased background signal in *in vivo* imaging.

We also studied the capability for *in vivo* biodegradation. Mice implanted with 2 mg/mL PGNs were imaged after implantation (Figure 7A) and 1 day later (Figure 7B). As expected, the matrigel and saline carriers were largely resorbed into circulation and extracellular matrix. Concurrently, the PGNs implanted began to degrade; we observed a 3.5-fold decrease in signal-to-background after 1 day (Figure 7D).

A final study labeled MSCs with the PGNs. We first optimized the labeling protocol using the cell fluorescence to monitor labeling. There was a linear relationship ($R^2 = 0.98$) between the starting concentration and the resulting cell fluorescence from 30 to 1000 μg/mL of PGNs at 2 h of incubation. When the incubation time was optimized from 1 to 360 min at 500 μg/mL, a marked plateau effect was noted after 1 h of incubation. Further incubation with cells did not significantly increase cell signal ($p > 0.05$). Even 30 min of incubation gave cell signals that were 70% of the maximum. We used these conditions to label MSCs and then imaged them with ultrasound (Figure 8C) and fluorescence microscopy (Figure 8D).

We next used microscopy to understand the interaction of the PGNs with the MSC. Epifluorescence

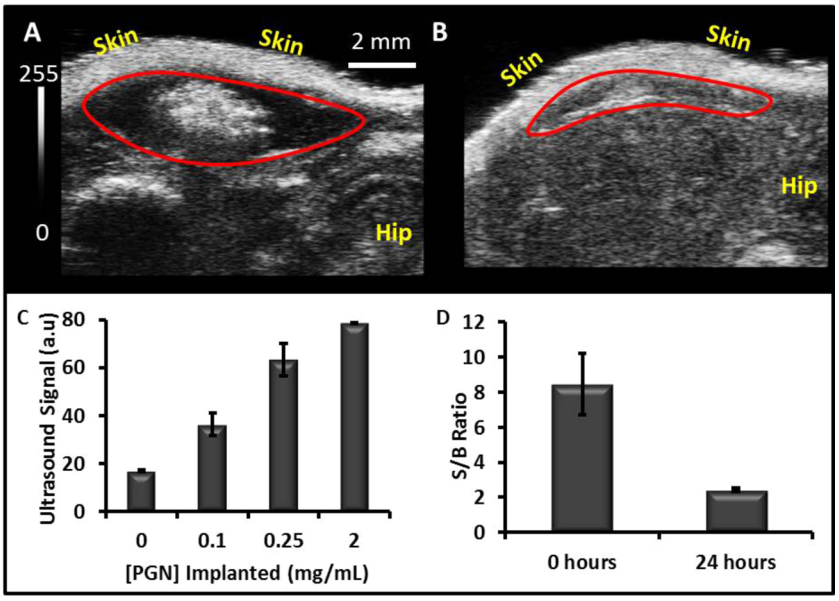

Figure 7. *In vivo* **imaging with PGNs. Nu/nu mice received 100 μL boluses of 2 mg/mL PGNs in 1:1 matrigel:PBS and imaged at 40 MHz immediately after (A) and 1 day after (B). Red outlines in A and B indicate the region of implantation, and the scale bar and intensity bar in A apply to both panels. (C) Decreasing concentrations of PGNs were also implanted to calculate the limit of detection and variance between animals. Error bars represent the standard error of measurement. (D) Changes in ultrasound backscatter for PGNs indicate a 3.5-fold decrease in signal-to-background ratio (SBR). Error bars represent the standard deviation.**

microscopy indicated low nonspecific binding of PGNs to the culture flaks. Indeed, <5% of the fluorescent pixels do not correspond to a cell in Figure 8E with many regions of increased signal throughout the MSC.

We also used confocal microscopy to study the distribution of the PGNs. Our goal was to determine whether the nanoparticles were on the cells or inside the cells. This is important because nanoparticles that were only on the surface could become detached after implant and incorrectly be considered a cell. The confocal data in Figure 8K shows that the nanoparticles are indeed located throughout the cell in the cytoplasm and are not simply on the cell surface.

Finally, we placed different numbers of cells in a 100 μL inclusion in an agar phantom and imaged at 40 MHz. We used this cell volume because it is similar to the injection volume used in trials of nonhuman primates and would likely be used in man. We noted a a linear relationship between the number of cells and the ultrasound backscatter ($R_2 > 0.99$; Figure 8C), which is important for studies in which unknown numbers of cells may need to be quantitated. The calculated limit of detection for ultrasound imaging was 4000 MSCs at three standard deviations above the mean of the background.

DISCUSSION

In the present study, we take advantage of the sol–gel preparation method to synthesize controlled degradation materials and the subsequent utility of electrospraying to prepare ternary phosphate-based sol–gel derived glass nanospheres in the diameter size range of 200–500 nm. One limitation of this approach is throughput *versus* "bottom-up" nanoparticles synthetic approaches; however, we were able to produce 60 mg of nanoparticles per hour, which is sufficient for imaging experiments. Previous approaches to preparing these glasses have been focused on preparing bulk sol–gel glasses. However, the slow sol–gel reaction and difficulty in making bulk glasses have limited their biomedical applications. In our work, faster reactive precursors and lower heat-treatment temperature were applied that allowed us to process these sol–gel derived glasses *via* electrospraying and also incorporate fluorescein dye while processing (due to the relatively benign processing temperatures).

The amorphous nature of these PGNs was confirmed by XRD analysis. The ^{31}P MAS NMR, and FTIR results also show the structure of these PGNs consists of mainly Q^1 and Q^2 phosphate units. These findings confirm the amorphous and glassy structure of the PGNs that are more desirable as a biodegradable material because they do not fragment during the degradation, which may cause inflammation.[32]

The PGNs have strong ultrasound backscattering capabilities both *in vivo* and *in vitro*. Phantom experiments indicated a limit of detection of 5 μg/mL with linear behavior below 1000 μg/mL (Figure 6A). The imaging window of this material is below 4 h. The ICP data show the highest rate of dissolution within the first 12 h of immersion in distilled water (Figure 4), and our time course study shows that by 4 h the signal has decreased more than 2-fold with even further decreases the next day (Figure 6D). This is particularly

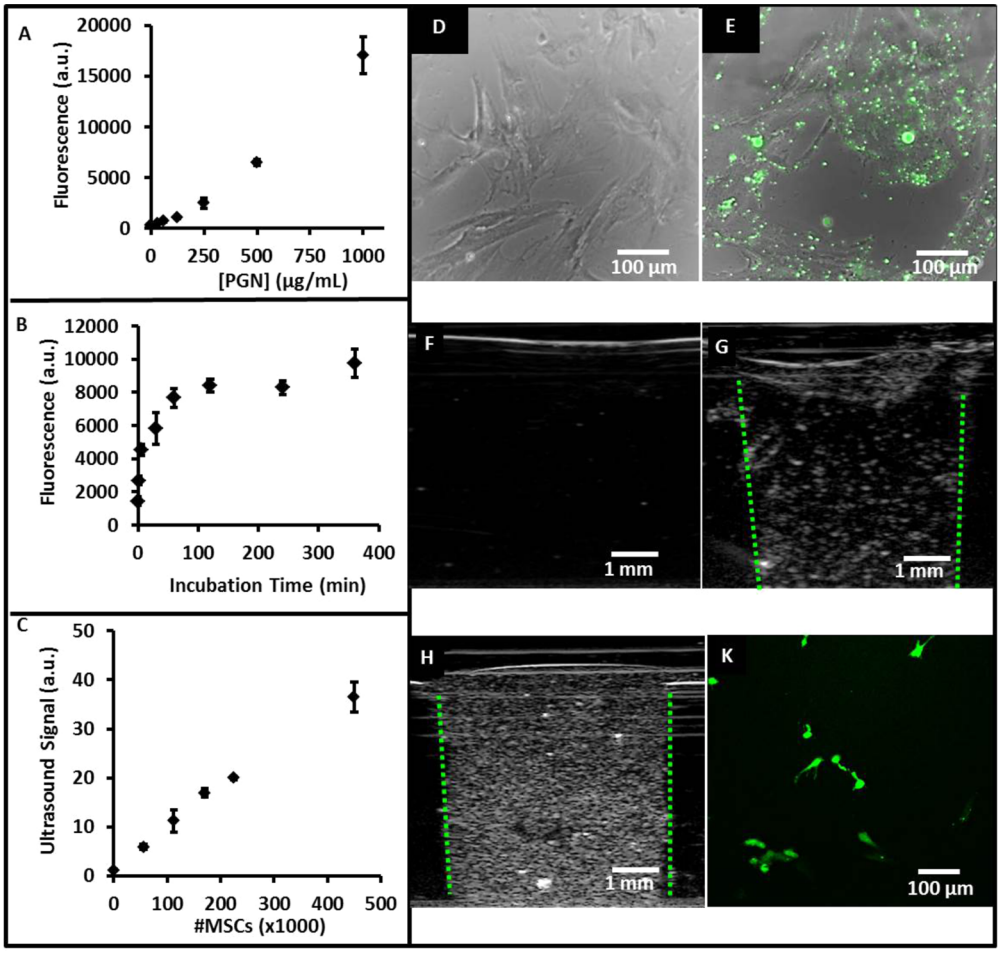

Figure 8. PGN-labeled MSCs. The optimal labeling conditions were tested empirically including starting concentration of PGNs (A) and incubation time (B). We found a nearly linear relationship between starting concentration and cell fluorescence (A). These concentrations used 2 h of labeling.(B) Effect of time indiates incubation times beyond 2 h offered no additional signal. (C) MSCs labeled with these conditions (500 μg/mL and 2 h) were imaged with 40 MHz ultrasound; the limit of detection is 4000 MSCs. Phase contrast/fluorescence microscopy of naive MSCs (D), and MSCs labeled with PGNs shows that fluorescence only corresponds to the cells (low nonspecific binding) (E). (F) Ultrasound image of agarose phantom only (no cells); (G) ultrasound backscatter from 225000 MSCs; (H) same number of MSCs labeled with PGNs in an agar phantom. The PGNs increased the backscatter 2-fold *versus* unlabeled cells. (K) Confocal image through the medial slice of adherent cells labeled with fluorescently tagged PGNs. The image shows that the nanoparticles are located throughout the cell and are localized in the cytoplasm and are not simply on the cell surface.

important because it bridges a gap between the minutes of stability of microbubbles and the months of stability of Stober silica particles.[33,34]

One potential concern is that the high local ionic concentrations could perturb cellular function. For 0.1 mg/mL of PGNs, over the 48 h of dissolution study and assuming no diffusion, cells would be exposed to 41 ppm of $(PO_4)^{3-}$, 32 ppm of Ca^{2+}, and 16 ppm of Na^{+} (Figure 4). These values are well within the standard physiological range of serum chemistries.[35] For example, the reference range of Ca^{2+} is 8.5−10 mg/dL or 85−100 ppm. The additional calcium due to the contrast agents is within the reference range and will not perturb cell metabolism. Furthermore, diffusion and normal circulation will equilibrate any locally disturbed ionic concentrations.

To further confirm this, we performed a series of cell toxicity assays. While we did find that very high doses (1000 μg/mL) increased ROS (hydroxyl, peroxyl, *etc.*) activity within the cell, this is much higher than the concentrations needed for imaging: 250 μg/mL for MSC imaging and >9 μg/mL for subcutaneous imaging (Figure 5A). All materials, even water, are toxic at some concentration; our goal here was to discover what concentration began to dysregulates metabolism and work below that concentration. After PGNs implantation into animals, we noticed no changes in posture, behavior, gait, or feeding with observation up to 2 weeks.

We also used the MTS assay to study cell metabolism and viability *via* mitochondrial reductase activity (Figure 5). MTS is a colorimetric, water-soluble tetrazolium dye that indicates the activity of oxidoreductase enzymes. One concern was that the degradation products may increase the sodium, calcium, and phosphorus concentration to levels inconsistent with

cell survival. Thus, it was important for us to study both fresh and degraded PGNs in this assay. Fortunately, we noticed no cytotoxicity in either sample group at concentrations below 500 μg/mL (Figure 5).

Although we did not investigate tumor imaging here, the PGNs implantation experiments (Figure 7) indicated that concentrations down to 9 μg/mL could be imaged *in vivo*. This is important because nanoparticle contrast agents must overcome significant competition from the reticuloendothelial system to reach target tissue. Values near 4% ID/g are common for nanoparticle contrast agents. Thus, a 1 g tumor would need at least 225 μg of material injected into the 2.5 mL murine blood pool to achieve 4% ID/g accumulation. Importantly, this concentration is well below the concentration that increased ROS generation.

Our primary goal was cell imaging, which is critical to understand the location of implanted stem cells in regenerative medicine. We achieved cell counting below 5000 cells in 100 μL volumes (Figure 8). While we do not achieve the single cell counts possible with some MRI techniques,[36] the cell counts described here are more than sufficient for clinical trials that will likely use millions of cells.[37−39] These low detection limits would be useful because they would allow one to not label all cells in a given population. The 4 h imaging window would be useful for imaging the immediate implantation event in cells. Long-term imaging could utilize a reporter gene.[40]

The detection limits reported here are higher than that achieved with perfluorocarbon microbubbles. Indeed, these can be detected even at the single microbubble level.[41] The PGNs will definitely not be detectable at the single particle level, but did have detection levels down to 50 μg/mL, which is on par with the 20 μg/mL detection limits we have reported previously with silica nanoparticles.[14] These materials also have lower overall signal intensity than perfluorocarbon microbubbles. However, perfluorocarbon microbubbles are approximately the same size as cells, and using them for ultrasound cell imaging is difficult. Importantly, the PGNs are approximately 10-fold smaller in diameter (and 1000-fold smaller in volume) and thus have a significant advantage for ultrasound cell imaging. In addition, the time stability of the PGNs (~4 h) is much longer than the minutes of *in vivo* stability for perfluorocarbon microbubbles.

CONCLUSION

In this study, for the first time, according to our knowledge, ternary phosphate-based sol−gel glass nanospheres in the diameter size range of 200−500 nm have been successfully prepared. The amorphous and glassy nature of these PGNs was confirmed *via* XRD, ^{31}P MAS NMR, and FTIR analysis. This probe is useful for both *in vivo* and *in vitro* ultrasound imaging and has utility for cell-tracking applications in regenerative medicine. Future work may utilize these contrast agents for tasks beyond regenerative medicine including targeted tumor imaging after iv injection and tumor imaging.

MATERIALS AND METHODS

Synthesis of the Sol for Subsequent Electrospraying. The following chemical precursors were used without further purification: triethyl phosphate (Aldrich, 99%), calcium methoxyethoxide (Ca-methoxyethoxide, ABCR, 20% in methoxyethanol), sodium methoxide solution (NaOMe, Aldrich, 30 wt % in methanol), 2-methoxyethanol (MeO-EtOH, Aldrich, 99.8%), *n*-dimethylformamide (nDMF, Alfa-Aesar, 99.8%), acetone (Alfa-Aesar, 99.5%), fluorescein (Aldrich), and silicone oil (Aldrich).

The sol−gel synthesis was begun by diluting triethyl phosphate in MeO-EtOH at a molar ratio of 1:3 and allowing them to react for about 10 min while the solution was magnetically stirred (the whole reaction being carried out in a dried vessel). The vessel was then cooled in an ice-bath before adding Ca-methoxyethoxide and NaOMe dropwise to the vessel. Finally, in the last stage, n-DMF (a molar ratio of 0.25:1) was added to the solution and a homogeneous solution was obtained after 10 min of stirring. For labeling experiments, 1 wt % fluorescein dye was incorporated to a subset of the mixture.

Electrospraying. The mixtures were aged overnight at 60 °C before being electrosprayed over the heated silicone oil. The electrospraying technique used a stainless steel capillary tube (18 gauge), syringe pump, high voltage source, and silicone oil as a substrate. The distance between the nozzle and substrate was 10 cm, and the temperature of the substrate was controlled and kept at 150 °C. The flow rate was 0.20 mL h^{-1}, and a high voltage of 20 kV was applied between the nozzle and the ground. The particles were separated from silicone oil *via* centrifugation at 4600 rpm for 30 min. The collected particles were washed three times with acetone and then dried at 180 °C for 2 h to evaporate the acetone and other remaining solvents.

Characterization. *SEM and EDX.* SEM images were obtained on a Philips-XL30 instrument (Philips, Netherland) at an accelerating voltage of 5 kV and working distance of 10 mm. The PGNs were mounted onto a stub using Araldite and sputter-coated with gold alloys. The diameter was measured for more than 100 particles using Image-pro plus software (Media Cybernetics, USA). To determine the exact composition of the PGNs, EDX-Inca 300 (Oxford instrument, UK) was used. Scanning electron microscopy (SEM)-XL30 was operated at 20 kV, spot size 5, and a working distance of 10 mm to identify the particular elements and their relative proportions from the scanned area.

XRD and ^{31}P MAS NMR. The XRD on PGNs was obtained on a Bruker-D8 Advance Diffractometer (Brüker, UK) in a flat plate geometry using Ni-filtered Cu Kα radiation. Data were collected using a Lynx Eye detector with a step size of 0.02° over an angular range of 2θ = 10−100° and a count time of 12 s.

The solid-state ^{31}P MAS NMR spectrum was recorded at 161.87 MHz using a Varian VNMRS-400 spectrometer. The sample was loaded into a 4 mm (rotor o.d.) magic angle spinning probe, and the spectrum was obtained using direct excitation (with a 90° pulse) with a 60 s recycle delay at ambient probe temperature (~25 °C) at a sample spin rate of 10 kHz. Between 20 and 88 repetitions were accumulated. The deconvolution of the spectrum was carried out using DMFit software, and was referenced to the resonance of the ammonium dihydrogen phosphate ($NH_4H_2PO_4$) at 0.9 ppm (relative to 85% H_3PO_4 solution at 0 ppm).[42]

FTIR. The FTIR spectrum of PGNs was collected using a PerkinElmer spectrometer 2000 (USA). The sample was scanned at room temperature in the absorbance mode in the range 1500−600 cm^{-1}, and the data were analyzed by PerkinElmer software.

Tissue Culture, Labeling, and Cytotoxicity. Mesenchymal stem cells (MSCs) and culture media were purchased from Lonza (p/n 2501 and 3001, respectively). Cells were seeded at 5000 cells/cm^2, and the media was changed every 2−3 days. Cell labeling used MSCs plated at 5000 cells/cm^2 in a 225 cm^2 flask and grown to 80% confluence. For labeling optimization studies, we used 12-well plates and the same seeding density. The day of labeling, we prepared the PGN contrast agent in PBS at 25 mg/mL. For optimizing the labeling experiments, decreasing volumes of this sample were then added to MSCs in media. The cells were exposed to PGN concentrations of 30−1000 μg/mL in the media; the NPs were then incubated with the cells for 2 h and then washed three times with PBS. To study the effect of time, we used 500 μg/mL of PGNs from 1 to 360 min. For labeling experiments, we used fluorescently tagged PGNs. Cell fluorescence was measured with a plate reader (Bio-TEK), and fluorescence microscopy used a EVOS Fl (Invitrogen). Confocal microscopy used a Leica confocal microscope (TCS SP5) with a 20× APO objective (p/n 506147) seated on a Virbraplane air table. For z-stacking experiments, 20 slices were collected over ∼50 μm. A video was made by compiling the individual TIFF files into an .avi file.

For the cell counting experiments, we used the optimized protocol of 2 h and 250 μg/mL. After labeling, the cells were washed three times with saline. We monitored the washes with absorbance spectroscopy to confirm that the third wash contained no more nanoparticles. The cells were then removed from the flask with TrypLE Express (Invitrogen), washed with complete media to deactivate the trypsin, centrifuged at 300*g* at 4 °C for 5 min, and resuspended in saline. The cells were counted with an automated hemocytometer before being placed in a phantom and imaged.

For cell viability, cells were plated in a 96-well plate and allowed to adhere overnight. The next day, increasing concentrations of PGNs were added and allowed to incubate for 4 h. For a positive control, we added 10 μL of 1 mg/mL cetyltrimethylammonium bromide (CTAB) in phosphate-buffered saline. We assessed cell viability using the tetrazolium-based metabolic reagent compound 3-(4,5-dimethylthiazol-2-yl)-5-(3-carboxymethoxyphenyl)(4-sulfophenyl)-2*H*-tetrazolium (MTS; Promega). The solution was used as received: 20 μL of MTS solution was added to each well in a 96-well plate containing cells and allowed to incubate for 3 h. Absorbance at 490 nm was measured to estimate cell viability. Each condition was tested with at least four replicates.

To determine whether the particles generated any reactive oxygen species, we utilized 2′,7′-dichlorofluorescein diacetate (DCFDA; Biotium). We first made a 1 mg/mL working solution of DCFDA in dimethyl sulfoxide and then diluted 125 μL of the DMSO solution to 10 mL of Hanks buffered saline solution (HBSS). Cells were washed with fresh HBSS, and then 100 μL of the DCFDA solution in HBSS was added; the plate was incubated at 37 °C for 1 h. Next, the labeling solution was aspirated, and the cells were again washed with fresh HBSS. Increasing concentrations of particles in 100 μL were then added. Controls include 10% H_2O_2 and wells with no cells. The fluorescence of each well was measured 1 h later.

Biodegradation Monitoring. Biodegradation was monitored *via* inductively coupled plasma mass spectroscopy (ICP-MS). The experiment used 0.1 mg/mL samples in deionized water at 37 °C with three replicates at the following time points: 0, 0.2, 0.5, 1, 3, 6, 12, 24, and 48 h. The tubes were secured to a tube rotation device set to 5 rotations per minute. This device was in a 37 °C incubator under ambient humidity. After each time point, the resulting suspension was centrifuged at 4600 rpm for 30 min to separate the PGNs from the solution. The liquid phase was then extracted, and the PGNs were dried in the oven at 60 °C before they were resuspended in fresh deionized water. The release of calcium, phosphorus, and sodium in solution was measured by using a Spectro Mass 2000 Analytical System calibrated across the predicted concentrations range −4000 ppb by dilution of 100 ppm elemental standards. Calcium standard was obtained as part of a premade standard solution (Fluka), whereas phosphorus and sodium standards were created from analytical grade K_2HPO_4 (Sigma) and $NaNO_3$ (Sigma) salts, respectively. Standards were first diluted in deionized water to result in the desired concentration range. Both samples and standards were diluted in 1:1 in 4% HNO_3 (Fluka) and analyzed in reference to a blank (2% HNO_3) solution under standard operating conditions (Power: 1350 W; Coolant Flow: 15 L/min: Auxiliary Flow: 1 L/min). Results were expressed as a cumulative ion release over the full period of the degradation study.

In Vitro Ultrasound Imaging. To measure the echogenicity of the nanoparticles, we placed increasing concentrations in a 1% agarose phantom. Ultrasound backscatter mode (B-mode) images were collected with a Visualsonics 2100 scanner with a MS-550 transducer (Fuji) for 40 MHz center frequency imaging or a MS-250 transducer for 16 MHz. Other imaging parameters included 100% power, 35 dB gain, and a 60 dB dynamic range. At least three frames were collected for each sample and saved as TIFF files, and were quantitated with ImageJ software using region of interest analysis and 8-bit depth as the dependent variable (0−255).[43] To calculate the limit of detection, we used three standard deviations above the mean of the blank.

In Vivo Ultrasound Imaging. All animal studies were approved by the Administrative Panel for Laboratory Animal Care (IACUC) at Stanford University. Nude mice aged 10−14 weeks were anaesthetized with 2% isofluorane in oxygen at 2 L/min. The PGNs were dissolved in 50:50 matrigel:PBS at 2.0, 0.25, and 0.1 mg/mL. The injection volume was 100 μL, which was subcutaneously implanted on the rear flank of the mice. The animals were imaged 10 min after implantation after the matrigel had solidified using 40 MHz center frequency, 100% power, 35 dB gain, and a 60 dB dynamic range. At least three frames were collected for each sample and saved as TIFF files, and images were quantitated with ImageJ. For longitudinal imaging, the injection site was marked and the animal returned to the same position the next day for identical imaging conditions.

Conflict of Interest: The authors declare no competing financial interest.

Acknowledgment. J.V.J. acknowledges support from NHLBI (K99-HL117048) and the Burroughs Wellcome Fund (1011172). Instrumentation used in this work was supported by NIH Grant No. S10-OD010344. This work was supported in part by the Priority Research Centers Program (No. 2009-0093829) through the National Research Foundation, Republic of Korea. We thank the EPSRC NMR Service at the Chemistry Department, Durham University, for the MAS NMR measurement.

REFERENCES AND NOTES

1. Goldberg, B. B.; Liu, J. B. Contrast Agents in Abdominal Ultrasound. *Front Gastroint Res.* **1997**, *24*, 323–341.
2. Benchimol, M. J.; Hsu, M. J.; Schutt, C. E.; Hall, D. J.; Mattrey, R. F.; Esener, S. C. Phospholipid/Carbocyanine Dye-Shelled Microbubbles as Ultrasound-Modulated Fluorescent Contrast Agents. *Soft Matter* **2013**, *9*, 2384–2388.
3. Nakatsuka, M. A.; Hsu, M. J.; Esener, S. C.; Cha, J. N.; Goodwin, A. P. DNA-Coated Microbubbles with Biochemically Tunable Ultrasound Contrast Activity. *Adv. Mater.* **2011**, *23*, 4908–4912.
4. Willmann, J. K.; Paulmurugan, R.; Chen, K.; Gheysens, O.; Rodriguez-Porcel, M.; Lutz, A. M.; Chen, I. Y.; Chen, X.; Gambhir, S. S. Us Imaging of Tumor Angiogenesis with Microbubbles Targeted to Vascular Endothelial Growth Factor Receptor Type 2 in Mice. *Radiology* **2008**, *246*, 508–518.
5. Gramiak, R.; Shah, P. M. Echocardiography of the Aortic Root. *Invest. Radiol.* **1968**, *3*, 356–366.
6. Klibanov, A. L. Targeted Delivery of Gas-Filled Microspheres, Contrast Agents for Ultrasound Imaging. *Adv. Drug Delivery Rev.* **1999**, *37*, 139–157.

7. Schutt, E. G.; Klein, D. H.; Mattrey, R. M.; Riess, J. G. Injectable Microbubbles as Contrast Agents for Diagnostic Ultrasound Imaging: The Key Role of Perfluorochemicals. *Angew. Chem., Int. Ed.* **2003**, *42*, 3218–3235.
8. Kono, Y.; Holscher, T.; Mattrey, R. F. Use of Ultrasound Microbubbles for Vascular Imaging. *Fund. Biomed. Technol.* **2008**, 311–325.
9. Klibanov, A. L. Ligand-Carrying Gas-Filled Microbubbles: Ultrasound Contrast Agents for Targeted Molecular Imaging. *Bioconjugate Chem.* **2005**, *16*, 9–17.
10. Xing, Z. W.; Wang, J. R.; Ke, H. T.; Zhao, B.; Yue, X. L.; Dai, Z. F.; Liu, J. B. The Fabrication of Novel Nanobubble Ultrasound Contrast Agent for Potential Tumor Imaging. *Nanotechnology* **2010**, 21.
11. Shapiro, M. G.; Goodwill, P. W.; Neogy, A.; Yin, M.; Foster, F. S.; Schaffer, D. V.; Conolly, S. M. Biogenic Gas Nanostructures as Ultrasonic Molecular Reporters. *Nat. Nanotechnol.* **2014**, *9*, 311–316.
12. Krupka, T. M.; Solorio, L.; Wilson, R. E.; Wu, H. P.; Azar, N.; Exner, A. A. Formulation and Characterization of Echogenic Lipid−Pluronic Nanobubbles. *Mol. Pharmaceut.* **2010**, *7*, 49–59.
13. Casciaro, S.; Conversano, F.; Ragusa, A.; Malvindi, M. A.; Franchini, R.; Greco, A.; Pellegrino, T.; Gigli, G. Optimal Enhancement Configuration of Silica Nanoparticles for Ultrasound Imaging and Automatic Detection at Conventional Diagnostic Frequencies. *Invest. Radiol.* **2010**, *45*, 715–724.
14. Jokerst, J. V.; Khademi, C.; Gambhir, S. S. Intracellular Aggregation of Multimodal Silica Nanoparticles for Ultrasound-Guided Stem Cell Implantation. *Sci. Transl. Med.* **2013**, 5.
15. Liberman, A.; Wu, Z.; Barback, C. V.; Viveros, R.; Blair, S. L.; Ellies, L. G.; Vera, D. R.; Mattrey, R. F.; Kummel, A. C.; Trogler, W. C. Color Doppler Ultrasound and Gamma Imaging of Intratumorally Injected 500 Nm Iron-Silica Nanoshells. *ACS Nano* **2013**, *7*, 6367–6377.
16. Ta, C. N.; Liberman, A.; Martinez, H. P.; Barback, C. V.; Mattrey, R. F.; Blair, S. L.; Trogler, W. C.; Kummel, A. C.; Wu, Z. Integrated Processing of Contrast Pulse Sequencing Ultrasound Imaging for Enhanced Active Contrast of Hollow Gas Filled Silica Nanoshells and Microshells. *J. Vac. Sci. Technol. B* **2012**, 30.
17. Martinez, H. P.; Kono, Y.; Blair, S. L.; Sandoval, S.; Wang-Rodriguez, J.; Mattrey, R. F.; Kummel, A. C.; Trogler, W. C. Hard Shell Gas-Filled Contrast Enhancement Particles for Colour Doppler Ultrasound Imaging of Tumors. *MedChemComm* **2010**, *1*, 266–270.
18. Malvindi, M. A.; Greco, A.; Conversano, F.; Figuerola, A.; Corti, M.; Bonora, M.; Lascialfari, A.; Doumari, H. A.; Moscardini, M.; Cingolani, R.; et al. Magnetic/Silica Nanocomposites as Dual-Mode Contrast Agents for Combined Magnetic Resonance Imaging and Ultrasonography. *Adv. Funct. Mater.* **2011**, *21*, 2548–2555.
19. Knowles, J. C. Phosphate Based Glasses for Biomedical Applications. *J. Mater. Chem.* **2003**, *13*, 2395.
20. Hench, L. L.; Polak, J. M. Third-Generation Biomedical Materials. *Science* **2002**, *295*, 1014.
21. Franks, K.; Abrahams, I.; Georgiou, G.; Knowles, J. C. Investigation of Thermal Parameters and Crystallisation in a Ternary CaO-Na_2O-P_2O_5-Based Glass System. *Biomaterials* **2001**, *22*, 497–501.
22. Pickup, D. M.; Guerry, P.; Moss, R. M.; Knowles, J. C.; Smith, M. E.; Newport, R. J. New Sol−Gel Synthesis of a $(CaO)_{0.3}(Na_2O)_{0.2}(P_2O_5)_{0.5}$ Bioresorbable Glass and Its Structural Characterisation. *J. Mater. Chem.* **2007**, *17*, 4777.
23. Lee, I. H.; Foroutan, F.; Lakhkar, N. J.; Gong, M. S.; Knowles, J. C. Sol−Gel Synthesis and Structural Characterization of P_2O_5-CaO-Na_2O Glasses. *Phys. Chem. Glasses-Eur. J. Glass Sci. Technol. Part B* **2013**, *54*, 115–120.
24. Carta, D.; Knowles, J. C.; Smith, M. E.; Newport, R. J. Synthesis and Structural Characterization of P_2O_5-CaO-Na_2O Sol−Gel Materials. *J. Non-Cryst. Solids* **2007**, *353*, 1141–1149.
25. Baia, L.; Muresan, D.; Baia, M.; Popp, J.; Simon, S. Structural Properties of Silver Nanoclusters-Phosphate Glass Composites. *Vib. Spectrosc.* **2007**, *43*, 313–318.
26. Byun, J. O.; Kim, B. H.; Hong, K. S.; Jung, H. J.; Lee, S. W.; Izyneev, A. A. Properties and Structure of RO-Na_2O-Al_2O_3-P_2O_5 (R = Mg, Ca, Sr, Ba) Glasses. *J. Non-Cryst. Solids* **1995**, *190*, 288–295.
27. Ilieva, D.; Jivov, B.; Kovacheva, D.; Tsacheva, T.; Dimitriev, Y.; Bogachev, G.; Petkov, C. Ft-Ir and Raman Spectra of Gd Phosphate Crystals and Glasses. *J. Non-Cryst. Solids* **2001**, *293*, 562–568.
28. Moustafa, Y. M.; El-Egili, K. Infrared Spectra of Sodium Phosphate Glasses. *J. Non-Cryst. Solids* **1998**, *240*, 144–153.
29. Sene, F. F.; Martinelli, J. R.; Gomes, L. Synthesis and Characterization of Niobium Phosphate Glasses Containing Barium and Potassium. *J. Non-Cryst. Solids* **2004**, *348*, 30–37.
30. Bunker, B. C.; Arnold, G. W.; Wilder, J. A. Phosphate-Glass Dissolution in Aqueous-Solutions. *J. Non-Cryst. Solids* **1984**, *64*, 291–316.
31. Hare, J. M.; Fishman, J. E.; Gerstenblith, G.; Velazquez, D. L. D.; Zambrano, J. P.; Suncion, V. Y.; Tracy, M.; Ghersin, E.; Johnston, P. V.; Brinker, J. A.; et al. Comparison of Allogeneic Vs Autologous Bone Marrow-Derived Mesenchymal Stem Cells Delivered by Transendocardial Injection in Patients with Ischemic Cardiomyopathy the Poseidon Randomized Trial. *JAMA, J. Am. Med. Assoc.* **2012**, *308*, 2369–2379.
32. Bostman, O. M.; Pihlajamaki, H. K. Adverse Tissue Reactions to Bioabsorbable Fixation Devices. *Clin. Orthop. Relat. R.* **2000**, 216–227.
33. Hudson, S. P.; Padera, R. F.; Langer, R.; Kohane, D. S. The Biocompatibility of Mesoporous Silicates. *Biomaterials* **2008**, *29*, 4045–4055.
34. He, Q. J.; Zhang, Z. W.; Gao, F.; Li, Y. P.; Shi, J. L. *In Vivo* Biodistribution and Urinary Excretion of Mesoporous Silica Nanoparticles: Effects of Particle Size and Pegylation. *Small* **2011**, *7*, 271–280.
35. Bishop, M. L. *Clinical Chemistry*, 6th ed.; Lippincott: Philadelphia, 2010.
36. Shapiro, E. M.; Sharer, K.; Skrtic, S.; Koretsky, A. P. *In Vivo* Detection of Single Cells by Mri. *Magn Reson Med.* **2006**, *55*, 242–249.
37. Chong, J. J. H.; Yang, X. L.; Don, C. W.; Minami, E.; Liu, Y. W.; Weyers, J. J.; Mahoney, W. M.; Van Biber, B.; Cook, S. M.; Palpant, N. J. Human Embryonic-Stem-Cell-Derived Cardiomyocytesregenerate Non-Humanprimate Hearts. *Nature* **2014**, *510*, 273.
38. Hare, J.; Fishman, J.; Gerstenblith, G. The Poseidon Randomized Trial. *JAMA, J. Am. Med. Assoc.* **2012**, *308*, 2369–2379.
39. Makkar, R. R.; Smith, R. R.; Cheng, K.; Malliaras, K.; Thomson, L. E.; Berman, D.; Czer, L. S.; Marbán, L.; Mendizabal, A.; Johnston, P. V. Intracoronary Cardiosphere-Derived Cells for Heart Regeneration after Myocardial Infarction (Caduceus): A Prospective, Randomised Phase 1 Trial. *Lancet* **2012**, *379*, 895–904.
40. Yaghoubi, S. S.; Couto, M. A.; Chen, C.-C.; Polavaram, L.; Cui, G.; Sen, L.; Gambhir, S. S. Preclinical Safety Evaluation of 18f-Fhbg: A Pet Reporter Probe for Imaging Herpes Simplex Virus Type 1 Thymidine Kinase (Hsv1-Tk) or Mutant Hsv1-Sr39tk's Expression. *J. Nucl. Med.* **2006**, *47*, 706–715.
41. Klibanov, A. L.; Rasche, P. T.; Hughes, M. S.; Wojdyla, J. K.; Galen, K. P.; Wible, J. H.; Brandenburger, G. H. Detection of Individual Microbubbles of Ultrasound Contrast Agents - Imaging of Free-Floating and Targeted Bubbles. *Invest Radiol* **2004**, *39*, 187–195.
42. Massiot, D.; Fayon, F.; Capron, M.; King, I.; Le Calv, S. p.; Alonso, B.; Durand, J.-O.; Bujoli, B.; Gan, Z.; Hoatson, G. Modelling One- and Two-Dimensional Solid-State NMR Spectra. *Magn. Reson. Chem.* **2002**, *40*, 70–76.
43. Schneider, C. A.; Rasband, W. S.; Eliceiri, K. W. NIH Image to ImageJ: 25 Years of Image Analysis. *Nat. Methods* **2012**, *9*, 671–675.